Title: **Energy based multiscale modeling with non-periodic boundary conditions**

Authors: Christopher Cater
Xinran Xiao

Report Documentation Page			*Form Approved* *OMB No. 0704-0188*

Public reporting burden for the collection of information is estimated to average 1 hour per response, including the time for reviewing instructions, searching existing data sources, gathering and maintaining the data needed, and completing and reviewing the collection of information. Send comments regarding this burden estimate or any other aspect of this collection of information, including suggestions for reducing this burden, to Washington Headquarters Services, Directorate for Information Operations and Reports, 1215 Jefferson Davis Highway, Suite 1204, Arlington VA 22202-4302. Respondents should be aware that notwithstanding any other provision of law, no person shall be subject to a penalty for failing to comply with a collection of information if it does not display a currently valid OMB control number.

1. REPORT DATE **13 MAY 2013**	2. REPORT TYPE **Journal Article**	3. DATES COVERED **07-01-2013 to 26-04-2013**

4. TITLE AND SUBTITLE **Energy based multiscale modeling with non-periodic boundary conditions**	5a. CONTRACT NUMBER **W56HZV-07-2-0001**
	5b. GRANT NUMBER
	5c. PROGRAM ELEMENT NUMBER
6. AUTHOR(S) **Christopher Cater; Xinran Xiao**	5d. PROJECT NUMBER
	5e. TASK NUMBER
	5f. WORK UNIT NUMBER

7. PERFORMING ORGANIZATION NAME(S) AND ADDRESS(ES) **Michigan State University,426 Auditorium Rd,East Lansing,Mi,48824**	8. PERFORMING ORGANIZATION REPORT NUMBER **; #23866**

9. SPONSORING/MONITORING AGENCY NAME(S) AND ADDRESS(ES) **U.S. Army TARDEC, 6501 East Eleven Mile Rd, Warren, Mi, 48397-5000**	10. SPONSOR/MONITOR'S ACRONYM(S) **TARDEC**
	11. SPONSOR/MONITOR'S REPORT NUMBER(S) **#23866**

12. DISTRIBUTION/AVAILABILITY STATEMENT
Approved for public release; distribution unlimited

13. SUPPLEMENTARY NOTES
Submitted to American Society for Composite Materials

14. ABSTRACT

The complex behavior and failure mechanisms of fiber-reinforced composite materials have made multiscale modeling a necessity when determining the response of composite structures. Current multiscale models, which bridge information between the microstructural constituents and the macroscopic response of a composite material are limited to a prescribed set of boundary conditions to kinematically link the macro and micro scales, with the most popular being periodic. This restriction prevents these types of models from accounting for the effects of locally non-periodic regions within a composite structure. One such region is a free-edge boundary, which is a common damage initiation zone for many composite structures. In this work, a semi-concurrent multiscale model is implemented within ABAQUS which allows for non-periodic boundary conditions through the development of an energy based constitutive coupling between the scales whereby Hill?s energy condition, or energetic consistency between the macro and micro scales, is preserved. The methodology is applied to examine free-edge effects on 2D lamina RVE?s with cohesive fiber/matrix failure within a semi-concurrent scheme.

15. SUBJECT TERMS

16. SECURITY CLASSIFICATION OF:			17. LIMITATION OF ABSTRACT	18. NUMBER OF PAGES	19a. NAME OF RESPONSIBLE PERSON
a. REPORT **unclassified**	b. ABSTRACT **unclassified**	c. THIS PAGE **unclassified**	**Public Release**	**22**	

ABSTRACT

The complex behavior and failure mechanisms of fiber-reinforced composite materials have made multiscale modeling a necessity when determining the response of composite structures. Current multiscale models, which bridge information between the microstructural constituents and the macroscopic response of a composite material, are limited to a prescribed set of boundary conditions to kinematically link the macro and micro scales, with the most popular being periodic. This restriction prevents these types of models from accounting for the effects of locally non-periodic regions within a composite structure. One such region is a free-edge boundary, which is a common damage initiation zone for many composite structures. In this work, a semi-concurrent multiscale model is implemented within ABAQUS which allows for non-periodic boundary conditions through the development of an energy based constitutive coupling between the scales whereby Hill's energy condition, or energetic consistency between the macro and micro scales, is preserved. The methodology is applied to examine free-edge effects on 2D lamina RVE's with cohesive fiber/matrix failure within a semi-concurrent scheme.

INTRODUCTION

The complex and hierarchical nature of composite materials make them highly desirable for high-performance and multi-functional applications. Consequently, the various length scales and reinforcement architectures present in a given composite pose a serious challenge for engineers and designers in predicting and modeling failure and damaged response [1]. Over the last several decades, a variety of multiscale methods have been developed to incorporate the effects of the composite microstructure on the overall macroscopic behavior [2]. Available multiscale models can be classified into three generic categories: sequential, concurrent, and semi-concurrent modeling [3]. These classifications are presented schematically in Figure 1.

Sequential models include standard homogenization schemes which determine macroscopic material properties based on the composite microstructure and microconstituent properties [4–7]. These models, however, do not preserve microstructural information post-homogenization and only provide initial elastic

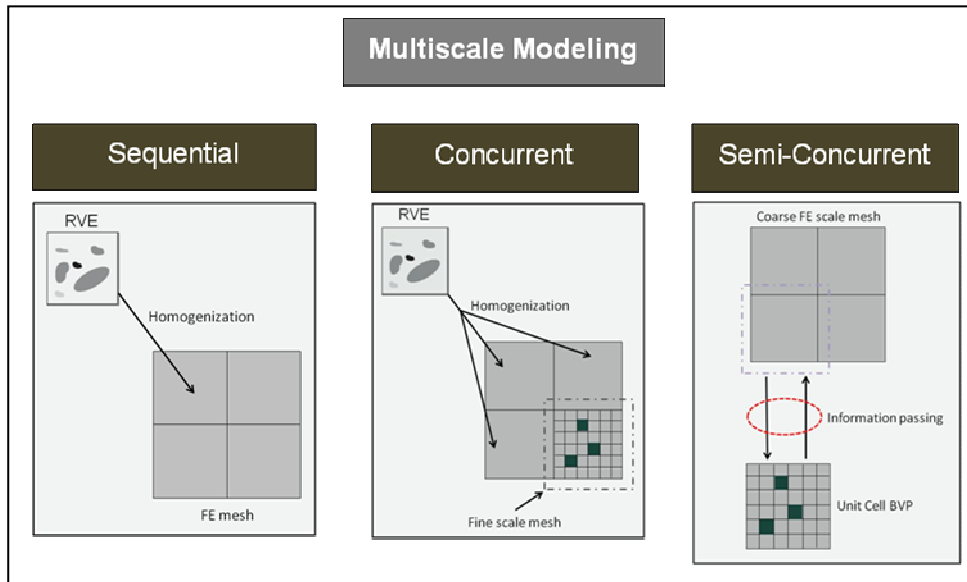Composite Vehicle Research Center, Michigan State University, 2727 Alliance Dr., Lansing, Michigan 48910

Figure 1: Classifications of multiscale methodologies

properties. Extrapolating the homogenized response to non-linear regions or determining composite failure will rely heavily on experimental tests to characterize material failure. While a variety of failure criteria exist at the homogenized scale of the lamina, or even the full laminate, the World Wide Failure Exercises (WWFE) have shown that no available models successfully capture UD failure under complex multi-axial loading states or for multi-ply laminates [8]. Concurrent models utilize domain decomposition, whereby detailed microstructural information is directly coupled at small regions of interest to a homogenized macroscopic domain [9–11]. A drawback of these methods is that the computational cost and memory requirements grow significantly with increasing size of the region of interest (i.e. due to large crack growth or diffuse damage). Additionally, adaptive remeshing schemes and transitionary elements are required to account for unknown *a-priori* damage paths and the coupling of multiple lengths scales in one FE mesh. Semi-concurrent models, on the other hand, preserve microstructural information by linking each integration point at the macroscopic level to a unique unit-cell boundary value problem (BVP) at the microscopic level [12–14]. The BVP, defined on a representative volume element (RVE), will determine the macroscopic response of the macroscopic integration point. This linking between the two scales is shown schematically in Figure 1, highlighting the passing of information between the weakly coupled scales. Despite the increased computational cost of semi-concurrent schemes over sequential methods, the uncoupled nature of each BVP allows for parallelization of the necessary microstructural solution.

The work presented utilizes a semi-concurrent, nested finite element (FE) methodology similar to that pioneered by Feyel and Chaboche [15], whereby the unit-cell BVP is solved using the FE method. In contrast to other semi-analytical methods [16,17], implementing a FE solution scheme allows for the implementation of explicit damage modeling through cohesive zone modeling [18,19] or through the extended-

Finite Element Method (XFEM) [3,20,21]. A significant limitation to current semi-concurrent models is the available boundary conditions with which one can drive the unit-cell BVP. While periodic boundary conditions have found to be effective over uniform displacement or uniform traction boundary conditions for determining the effective properties of an RVE [22,23], recent work by Coenen et al. [24] and Aboudi and Ryvkin [25] have shown that semi-concurrent models with periodic boundary conditions cannot capture the true material behavior in the presence of localized damage. Although a variety of novel boundary conditions have been presented in literature to overcome this limitation [24,26], the proposed boundary conditions are modified forms of periodicity and unable to account for strong non-periodic effects. The proposed work focuses on developing a methodology for implementing non-periodic boundary conditions in a semi-concurrent scheme while preserving energy between the scales.

MULTISCALE FRAMEWORK

The two main components in the semi-concurrent multiscale implementation are the localization and the homogenization rules. Localization refers to the passing of information from the homogenized global scale to local scale of the RVE. Conversely, homogenization refers to the determination of macroscopic quantities from the RVE, or the passing of information from RVE to the global integration point. In a deformation driven FE analysis, the localization rules provides the kinematic coupling from macroscopic to microscopic domains. Although the process can use the macroscopic strain at the selected integration point, the work that follows uses the macroscopic deformation gradient, F^M, as shown in Figure 2. The macroscopic deformation gradient is then used to specify necessary boundary conditions for the RVE's BVP. Standard procedures assume a volume average relationship between the deformation at the global scale and that of the RVE shown in Equation (1).

$$F_{ij}^M = \frac{1}{V_0} \int_{V_0} F_{ij}^m \, dV_0 \qquad (1)$$

The superscripts M and m represent macroscopic and microscopic quantities, respectively, F is the deformation gradient tensor, and V_0 is the reference volume of the RVE. The way in which the macroscopic deformation gradient provides boundary conditions (displacements, or u) on the RVE are provided in Equation (2),

$$u_i^m = \left(F_{ij}^M - I\right)X_j^m \qquad (2)$$

where X is the vector of reference configuration coordinates. The prescription of these displacements can be chosen for all nodes within the RVE, all nodes along the boundary, or restricted to the vertices in the case of periodicity. The homogenization procedure, which provides the macroscopic stress as a function of microscopic stresses, also involves an volume averaging relationship and is provided in Equation (3).

$$P_{ij}^M = \frac{1}{V_0} \int_{V_0} P_{ij}^m \, dV_0 \qquad (3)$$

The stress is written using the first Piola-Kirkhoff stress tensor, P , for convention, as it is the work conjugate to the deformation gradient. A second part of the

homogenization process is determining the instantaneous material Jacobian, J , shown in Figure 2.
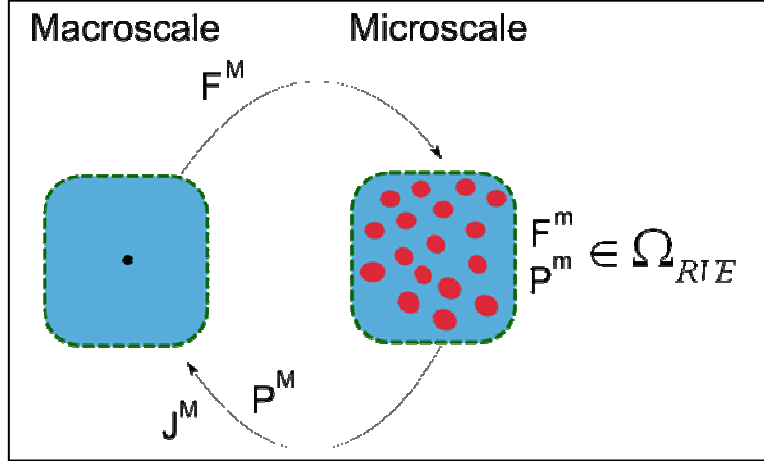

Figure 2. Overview of the semi-concurrent workflow and passing of information between the macroscale (global) and microscale (RVE/local).

PROPOSED Z-SCALAR METHOD

All multiscale schemes are required to preserve the Hill-Mandel relation which states that the variation of work at the global scale must equal the volume average of the variation of work at the local scale. This relation is shown graphically in Figure 3 as well as in Equation (4),

$$\delta W^M = \int_{V_0} \delta W^m \, dV_0 \tag{4}$$

where δW is the variation of work at a particular scale. As a result of the Hill-Mandel relation, the kinematic and constitutive coupling between the macroscopic and microscopic domain are constrained to satisfy the averaging relations provided in equations (1) and (3). These two equations state the volume average of the stress/strain field variables throughout the RVE are equal to the corresponding macroscopic variables. Given these averaging relations, it is a trivial calculation to show that the Hill-Mandel relation is satisfied, and these calculations are given for various types of RVE boundary conditions in work by Kouznetsova [12]. Coenen et al. [24] enforced boundary conditions satisfying the strain averaging relations, then proved that the volume averaged microscopic stress tensor would in fact satisfy the work equivalence between the scales. Equation (5) below expresses the Hill-Mandel relation in terms of the individual deformation gradient and stress tensors.

$$P_{ij}^M : \delta F_{ij}^M = \frac{1}{V_0} \int_{V_0} P^m : \delta F_{ij}^m \, dV_0, \qquad \forall \delta \vec{x} \tag{5}$$
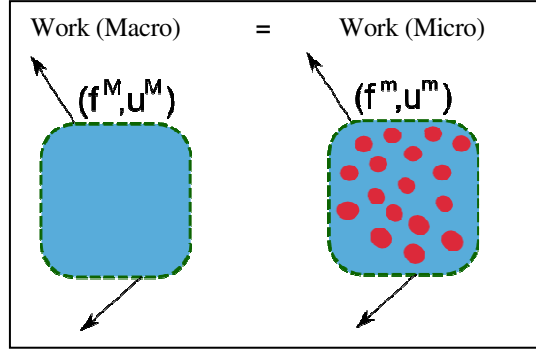
Figure 3. The work, or more precisely the variation of work, at both the macro and micro scales must be maintained for the multiscale scheme to be energetically consistent.

As was discussed in the work by Coenen et al. [24], the strain averaging relation (or alternatively, the deformation averaging relation) is satisfied when the contributions of the micro-fluctuation on the volume average are zero. A simplified form of this statement is shown in Equation (6),

$$F^M = \int_{\Omega_{RVE}} (\nabla_{0m} x^m) d\Omega_{RVE} = F^M + \int_{\Omega_{RVE}} (\nabla_{0m} \Delta w) \, d\Omega_{RVE} \qquad (6)$$

which is derived from the right hand side of Equation (1) and using Equation (7). It should be noted that the strain averaging relation is being written with respect to the deformation gradient rather than the strain tensor, however the equations still hold. The following relation

$$x_i^m = F_{ij}^M X_j^m + w_i \qquad (7)$$

describes the local, current coordinates x within the RVE as a function of the macroscopic deformation gradient and a function of the microfluctuation field, $\mathbf{w}$, which is dependent on the microstructure. This superposition of a macroscale influence and the microfluctuation field is graphically represented in Figure 4.

RVE deformation   **Macroscale influence**   **Microscale influence**
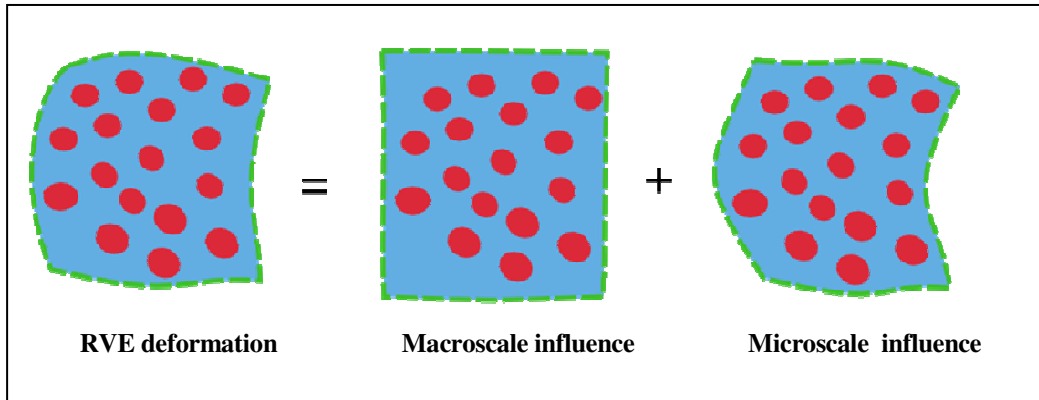
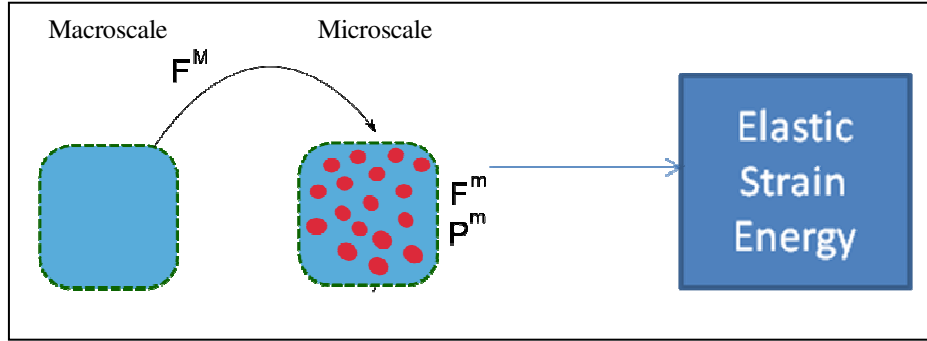Figure 4: Schematic of the RVE deformation as a superposition of macroscale and microscale influences.

Figure 5: Illustration of the localization process, which has deformed the RVE to produce a unique amount of elastic strain energy defined by the box on the right.

The strain, or deformation, averaging relation will only hold if last integral term in (6) is equal to zero. It has been shown in literature that periodic boundary conditions satisfy this requirement. Non-periodic, non-uniform boundary conditions, however, will contain a microscale influence field which will not set the integral term in (6) to be zero. The microscale influence field will be an unknown solution, dependent on the microstructure, thus the form of the macroscopic stress tensor cannot be solved analytically *a-priori*. Instead, it is assumed in this work that the volume average of the RVE stress field is a sufficient approximation, although there is no guarantee (due to the nature of the microfluctuation field) that it is consistent with Hill's energetic conditions.

In the first iteration of developing an energetically consistent stress tensor, an equivalence of elastic strain energy between the scales, as introduced by Hill [6], is directly enforced. First, the localization process is performed as in Figure 5 according to a given macroscopic quantity of deformation. At this stage, it is assumed that the localization provided a sufficient state of stress/strain within the RVE resulting in a given amount of elastic strain energy, shown by the blue box in Figure 5. It is desired to determine the macroscopic stress tensor required to ensure that the elastic strain energy at the global level matches that from the RVE. The formulation to follow assumes that the microconstituents are linear elastic with cohesive based interactions between the fibers and matrix. Due to the presence of elastic softening from the failing/failed cohesive surfaces, the elastic strain energy at the macroscopic level will be computed according to the diagram in Figure 6-(b), rather than the purely elastic case shown in Figure 6-(a). The 2D plane strain problem, to which this work is currently focused, requires that the elastic strain energy is computed from the contributions of stress and strain in the 3 degrees of freedom in the problem (11, 12, and 22 directions), shown in Figure 7. The condition of equivalent elastic strain energy between the scales enforces that the total energy shown in Figure 7 should be equal to that found during the localization process in Figure 5. Thus, this equality provides a constraint with which we can determine the form of the macroscopic stress. Although there are an infinite number of stress tensors, given known values of deformation

(strain) at the macroscopic level, that will satisfy the energy equivalence, it is hereby assumed that the macroscopic stress state can be approximated as being proportional to the volume average of the RVE stresses.
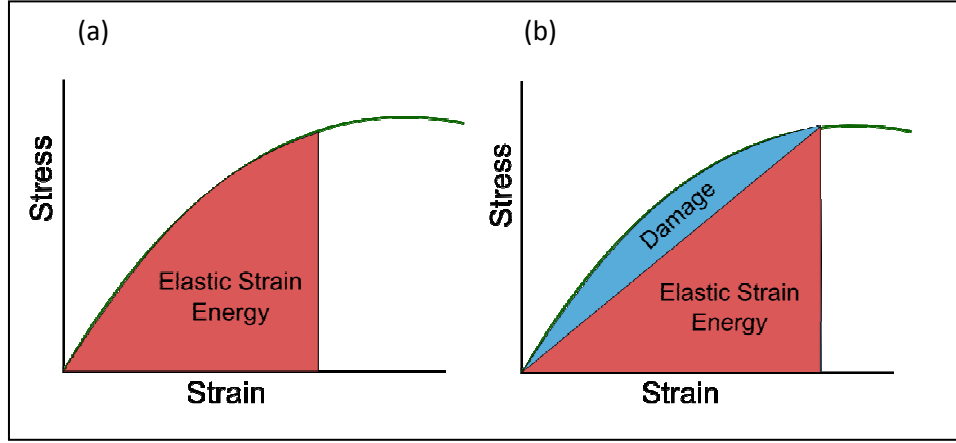

Figure 6: Stress-strain diagrams highlighting the elastic strain energy for two non-linear material responses where (a) the material is purely elastic and (b) the material has non-linearity due to elastic softening.

This assumption of proportionality introduces a scaling parameter, z, which will be found by enforcing energy equivalence between the global and local scale. The computation of the macroscopic stress tensor will now be found using

$$\sigma_{ij}^M = z * \sigma_{ij}^{\bullet M} = z * \frac{1}{V_0} \int_{V_0} \sigma_{ij}^m \, dV_0 \tag{8}$$

where $\sigma^{\bullet M}$ is the macroscopic Cauchy stress tensor computed from volume averaging the microscale Cauchy stress tensors, σ^m, in the RVE. The energy balance with respect to the elastic strain energy at the macro and micro scales can be written

$$E_{strain}^m = \left(\frac{1}{2}\epsilon_{11}^M\sigma_{11}^M + \frac{1}{2}\epsilon_{12}^M\sigma_{12}^M + \frac{1}{2}\epsilon_{22}^M\sigma_{22}^M\right) = z * \left(\frac{1}{2}\epsilon_{11}^M\sigma_{11}^{\bullet M} + \frac{1}{2}\epsilon_{12}^M\sigma_{12}^{\bullet M} + \frac{1}{2}\epsilon_{22}^M\sigma_{22}^{\bullet M}\right) \tag{9}$$

where left hand side represents the elastic strain energy at the microlevel, E_{strain}^m, from the RVE localization shown in Figure 5, while the right hand side represents the elastic strain energy computed using the volume averaged stresses. The z scalar parameter is computed using

$$z = \frac{2E_{strain}^m}{\left(\epsilon_{11}^M\sigma_{11}^{\bullet M} + \epsilon_{12}^M\sigma_{12}^{\bullet M} + \epsilon_{22}^M\sigma_{22}^{\bullet M}\right)} \tag{10}$$

where it is a function of the microscopic elastic strain energy, macroscopic strains, and volume averaged RVE stresses. This scalar parameter represents this energy based constitutive coupling between the microscopic and macroscopic scales. The next subsection will discuss the numerical implementation of this novel concept into the semi-concurrent scheme.
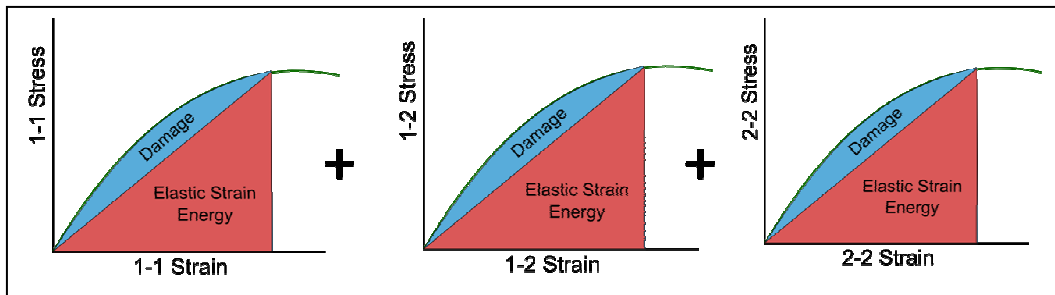
Figure 7: The total amount of elastic strain energy at the macroscopic level for the 2D plane strain problem is a summation of the elastic strain energy resulting from the three degrees of freedom.

NUMERICAL IMPLEMENTATION

The semi-concurrent scheme as well as the proposed z-scalar methodology was implemented numerically utilizing Python scripting to invoke the nested FE solution within the commercial FE software ABAQUS. To reduce initial overhead in implementing the multiscale framework the current model was restricted to 2D, plane strain analysis. The iterative algorithm is presented below in Figure 8. At each incremental step in the analysis, the user material defined subroutine (UMAT) was utilized to perform the communication between Python and the ABAQUS solver. The left-hand side of Figure 8 highlights the localization process which involves passing of the macroscopic deformation gradient from the UMAT to the custom Python script which then modifies the boundary conditions to a unit-cell, or RVE, ABAQUS input file. The unit-cell job is submitted and once completed is post-processed according to the right-hand side of Figure 8. As a test case for implementing non-periodic boundary conditions, a choice was made to implement boundary conditions equivalent to that shown in Figure 9-(a). These test boundary conditions contains a free edge at one boundary, corresponding to a macro scale with similar boundaries. The symmetric edge at the left of the RVE was an approximation chosen arbitrarily.
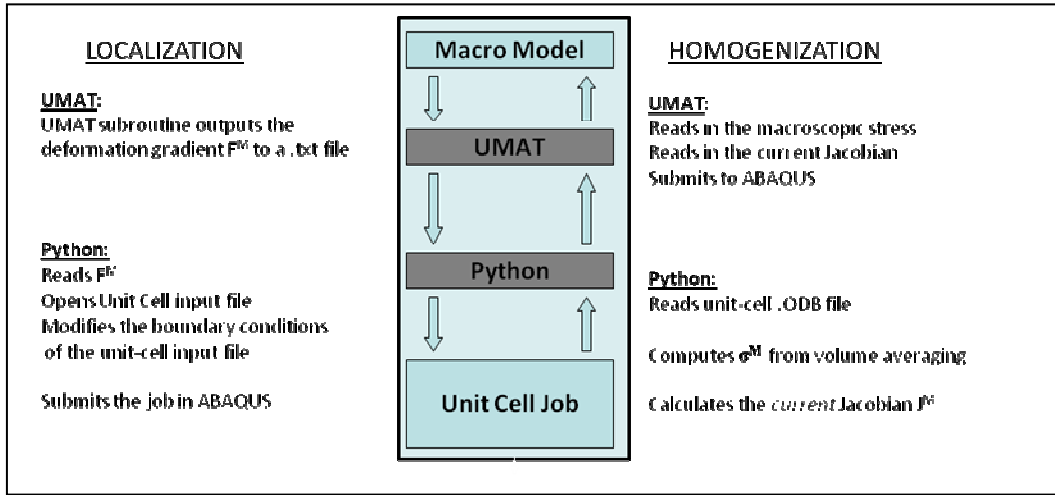
Figure 8: Workflow of the semi-concurrent computational homogenization scheme.
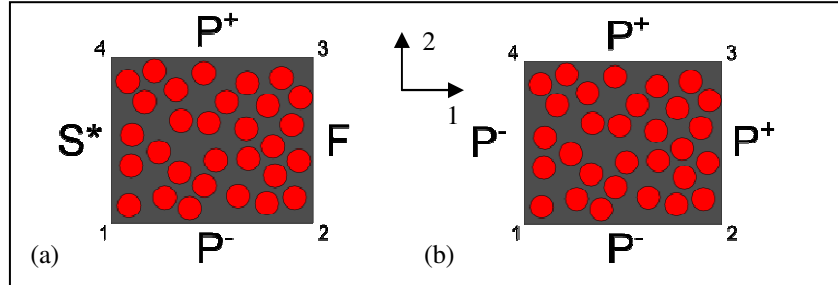

Figure 9: Schematic of (a) the test boundary conditions, which include the free edge, and (b) the standard periodic boundary conditions. Note: That P, F, S in the above diagram represent periodic, free and symmetric edge, respectively.

The implementation of the free-edge boundary conditions results in a different set of localization rules than those used for periodic boundary conditions given as

$$u_i^v = F_{ij}^M X_j^v \qquad (11)$$

The localization in equation (11) is identical to that in (2) except that the microscale displacements are only prescribed on the vertices, v, of the RVE. Elsewhere, non-vertex nodes are constrained to obey periodicity according to the formulation of Van der Sluis et al. [22] and using *Equation keywords in ABAQUS. In the case of the boundary conditions shown in Figure 9-(a), the localization shown in Equation (11) is prescribed for vertices 1 and 4. For vertices 2 and 3, displacements are only prescribed in the 2-direction to account for the free-edge requirement which must remain traction free in the 1-direction. Additionally, all nodes lying on the symmetric edge (S*) are prescribed displacements in the 1-direction and left undefined in the 2-direction.

1. Reads the EVOL, or current element volume for all elements
2. Extracts the element stresses within the unit-cell RVE
3. Computes the volume average of the stresses based on the EVOL values
4. Using the volume averaged stresses and Equation (10), z is calculated
5. The macroscopic stress tensor is exported to an external ".csv" file

Figure 10. Listing of the database post-processing steps performed in the custom Python script.

When implementing periodic boundary conditions, step 4 in Figure 10 is omitted. Aside from the macroscopic stress tensor, the material Jacobian needs to be determined for the subsequent increment in the global FE analysis and is a required output of the UMAT within ABAQUS Standard. The construction of the Jacobian from the perturbation steps is summarized in Figure 11. For a given perturbation step, a component of strain is set to unity, while all other are set to zero. Thus, the resulting stresses computed as a result provide a given column in the jacobian stiffness matrix. The stresses are computed using the same procedure as was done for the macroscopic stress tensor, utilizing the scaling parameter when necessary (e.g. when non-periodic localization is employed). The J_{33} component must be found externally using standard micromechanics, or basic homogenization techniques. Assuming the current type of RVE, little damage will be accumulating in the fiber direction, thus this component should remain a constant through the entire 2D analysis. The remaining components in the J_{X3} column are found assuming symmetry of the Jacobian. Once the Jacobian is computed and exported to a ".csv" file, the Python script is completed. The UMAT will then read in the macroscopic stress tensor and Jacobian which outputted back into the ABAQUS simulation at the global scale. When periodic boundary conditions are employed, the perturbation steps are executed immediately after the stress analysis within the same ABAQUS job. For the case of the test boundary conditions in Figure 9-(a), the operation must be performed as a separate unit-cell job after the completion of the stress analysis. Additionally, the boundary conditions are modified to remove the free-edge and are shown in Figure 12. The right-hand side of the RVE is perturbed using equation (11) for all nodes in both the 1- and 2-directions. The process for determining the Jacobian during the post-processing steps is listed in Figure 13. An overall summary of the discussed workflow with the Fortran subroutine and Python script are highlighted in Figure 14.

$$
\text{Set } \varepsilon_{11}=1 \qquad\qquad \text{Set } \varepsilon_{12}=1
$$

$$
\begin{bmatrix} \sigma_{11} \\ \sigma_{22} \\ \sigma_{33} \\ \sigma_{12} \end{bmatrix} = \begin{bmatrix} J_{11} & J_{12} & J_{13} & J_{14} \\ J_{21} & J_{22} & J_{23} & J_{24} \\ J_{31} & J_{32} & J_{33} & J_{34} \\ J_{41} & J_{42} & J_{43} & J_{44} \end{bmatrix} \begin{bmatrix} \varepsilon_{11} \\ \varepsilon_{22} \\ 0 \\ \varepsilon_{12} \end{bmatrix}
$$

Set $\varepsilon_{11} = 1$

Figure 11. The Jacobian matrix, **J**, is shown with the necessary uni-strain components for determining a particular column. The 33 component is determined externally.
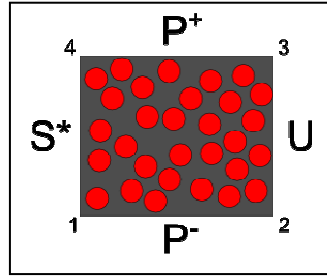

Figure 12. Boundary conditions used for the perturbation steps during non-periodic analysis.

6. Extract the nodal coordinates at the end of the localization step for all perturbed nodes
7. Use Equation (14) to determine BC's for the three perturbation steps
    Note: These steps are defined as linear perturbation steps in ABAQUS
8. Generate the necessary input file job and submit (Perturb.inp)
9. Compute the differential macroscopic stress tensor associated with each perturbation
10. Build the Jacobian and export the resultant to an external ".csv" file

Figure 13. Listing of the post-processing steps

Verification

The first step in verifying the modifications coded into the semi-concurrent scheme was to check the validity and robustness of the Jacobian updating procedure using the boundary conditions discussed in the previous section. This test was carried out by comparing computed elastic moduli (using Mathematica and the exported Jacobian matrices from Python) to those predicted from purely periodic boundary conditions. A number of test cases were examined including a homogeneous RVE, a single fiber RVE, and multi-fiber RVE. For the fiber/matrix RVE's the fiber volume fraction was 45%. Table I presents a comparison of the reference periodic values with those computed using the boundary conditions shown in Figure 12. For all three test cases, the non-periodic perturbations provided reasonable estimations of the material constants. It should be noted, however, that due to the uniform displacement boundary conditions on the right-hand side of the RVE caused the elastic moduli to be slighlty over-predictive.

TABLE I. Computed elastic constants for periodic and non-periodic perturbation steps.

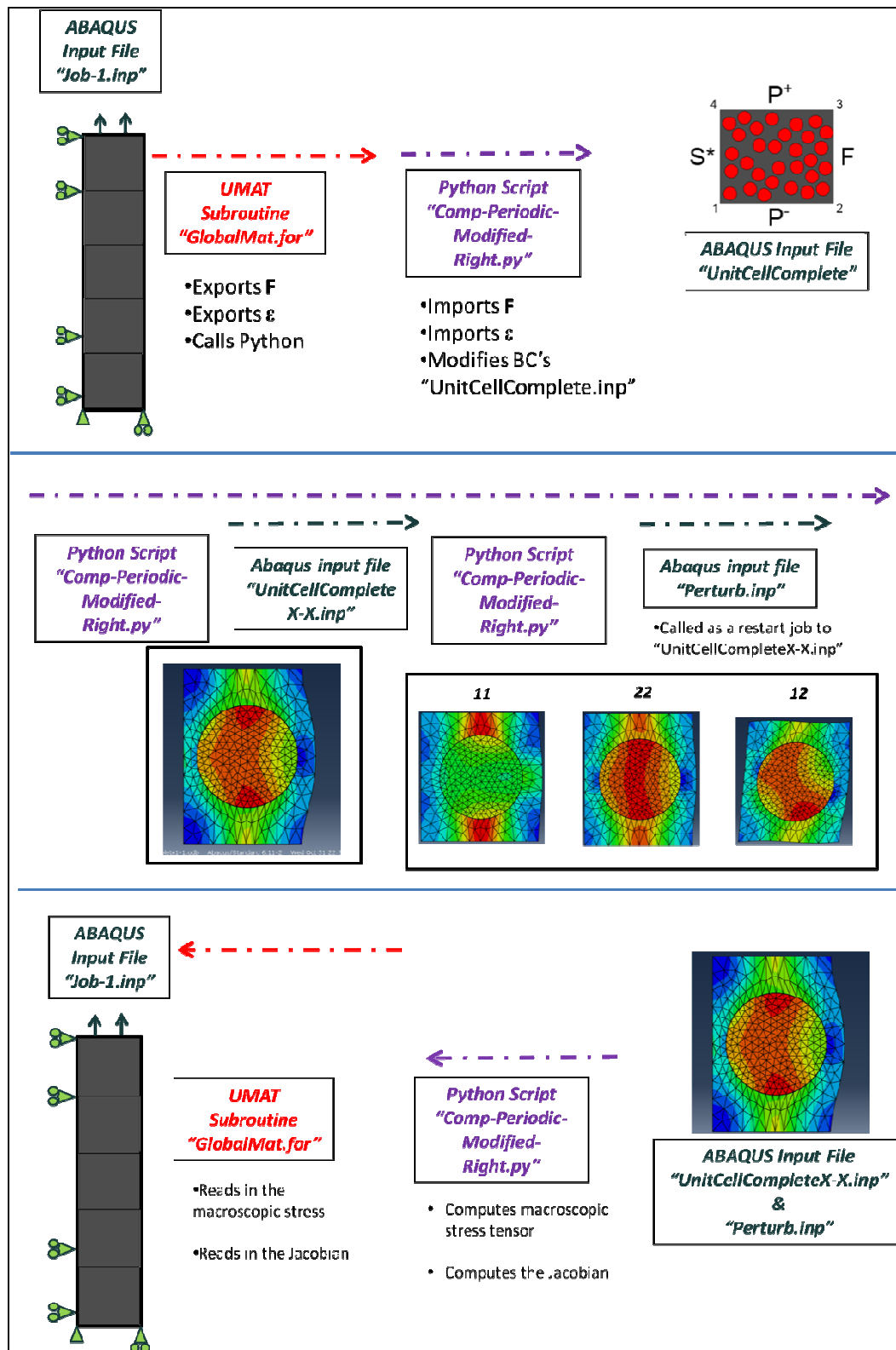| Material Constant	Homogeneous Solid		Single Fiber RVE (E_m = 3.5 GPa, E_f = 22GPa)		25-fiber RVE (E_m = 3.5 GPa, E_f = 22GPa)	
	Periodic	Non-Periodic	Periodic	Non-Periodic	Periodic	Non-Periodic
E_x (GPa)	100.00	100.000	20.897	21.257	20.247	20.455
E_y (GPa)	100.00	100.000	20.897	21.137	20.378	20.419
v_{xy}	0.300	0.300	0.294	0.295	0.330641	0.328911
G_{xy} (GPa)	38.462	38.462	6.438	6.901	7.207075	7.363027

Figure 14. Complete workflow of the numerical implementation of the non-periodic, semi-concurrent scheme.

The next step in the verification process was to confirm that the z-scalar method preserved energy between the global and local scales even when using non-periodic boundary conditions. A single, reduced-order quadrilateral element (CPE4R) at the global scale was placed under uniaxial tensile loading. The element's integration point was coupled to a 25 multi-fiber RVE with fibers placed randomly within the boundary of the RVE. Both periodic as well as the non-periodic free edge boundary conditions were employed in two separate iterations and the global elements were stretched to 1% strain. As was assumed in the formulation of the z-scalar method, all constituents are linear-elastic, however, a cohesive interface following a bilinear traction separation exists between the fiber and matrix. The necessary parameter for the cohesive interface are the cohesive strength, σ_{cohe} , and the critical displacement, d_{crit}. The cohesive strength defines the peak traction value in the traction-separation law, and the critical displacement specifies the traction-free separation distance. The cohesive parameters are chosen to be representative of a relatively weak interface. The constituent and interface properties are provided in Table II.

TABLE II. Constituent properties for the multi-fiber RVE verification study.

	E (GPa)	v	σ_{cohe} (MPa)	d_{crit} (m)
Fiber	22	0.3	--	--
Matrix	3.5	0.4	--	--
Interface	10E7	--	50	0.005

It was found during the verification studies that the ETOTAL, or total energy history variable, of the system was non-zero, a phenomenon that was indicative of incorrect energy computations. Figure 15 shows all the energy history variables outputted by ABAQUS. Further investigations revealed that the negative ETOTAL, highlighted by the dashed box in Figure 15, were a result of the contributions of the cohesive surface to the internal strain energy of the system. When using cohesive interactions rather than cohesive elements, the strain energy present in the separation of the fiber/matrix interface was not getting added to the total strain energy of the RVE system. Although the contribution of the cohesive interface to the strain energy of the system can be reduced by increasing the cohesive stiffness, even a sufficiently large value of 10E7 GPa had a measurable contribution as shown in Figure 15. Equation (12) shows the energy balance equations of relevant energy sources in the simulations.

$$E_{total} = E_{work} - E_{internal} = E_{work} - E_{stable} - E_{damage} - E_{Strain} \tag{12}$$

Due to the neglecting of cohesive strain energy, the E_{strain} , and consequently the $E_{internal}$, energy terms were being under reported resulting in a negative ETOTAL result.
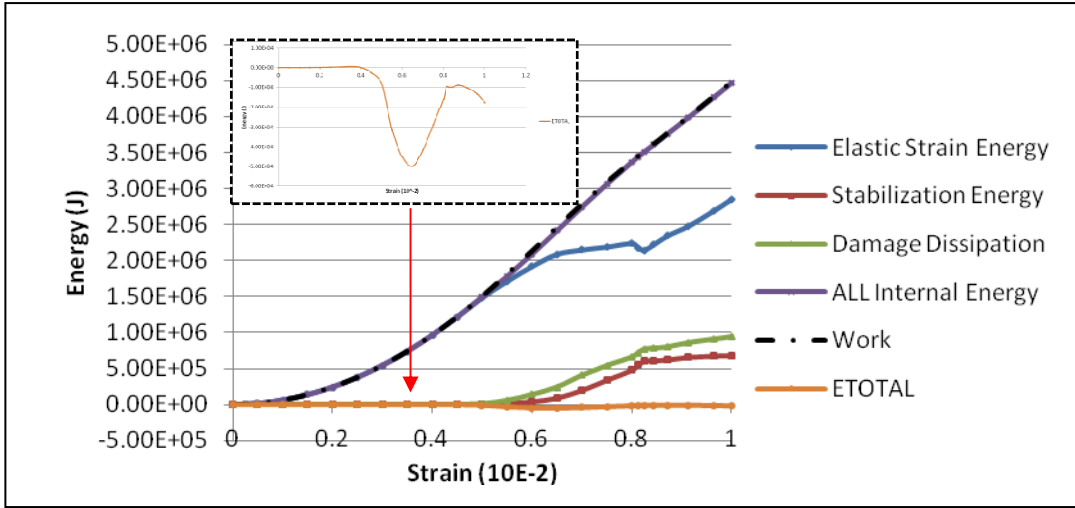
Figure 15. Energy history variable outputs for the 16 fiber RVE under periodic boundary conditions subject to uniaxial tensile loading.
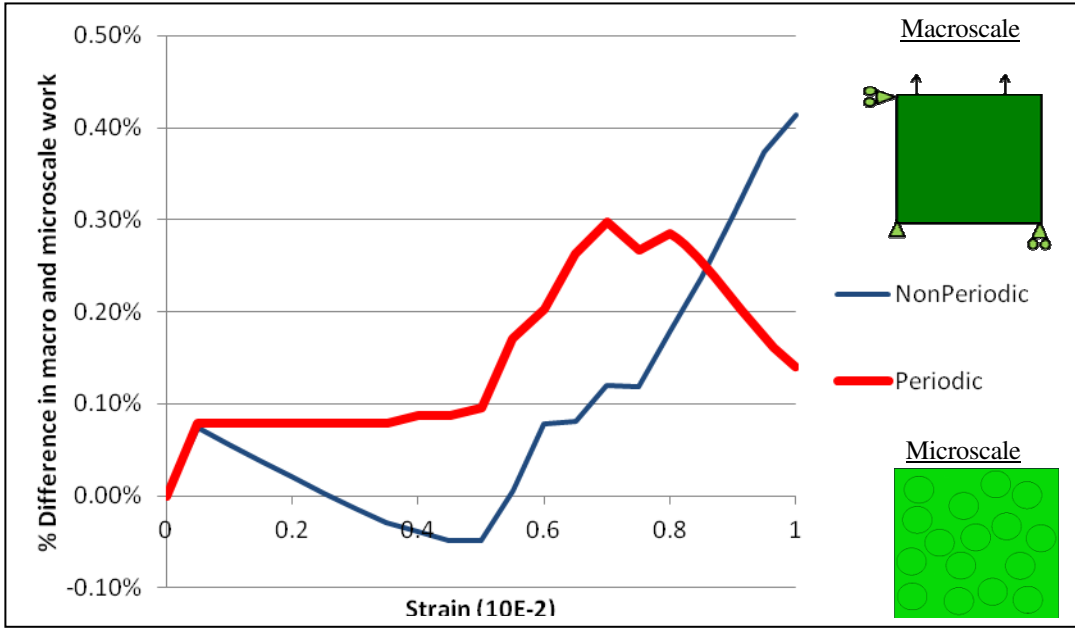
Figure 16. Percent difference in external work between the macro and micro scale work for the 16 fiber RVE for periodic and non-periodic boundary conditions.

As a consequence of the negative ETOTAL values, the computation of the z-scalar parameter in Equation (10) from the microstructural strain energy had to be modified as in

$$E_{strain}^m = E_{strain} - E_{total} \qquad (13)$$

The values E_{strain} and E_{total} in equation (13) were extracted from ABAQUS from the ALLE and ETOTAL history variables.

The results of the z-scalar verification are presented in Figure 16, plotting the percent difference in external work computed by ABAQUS between the global and local scales for the two boundary conditions cases (periodic and non-periodic with a free edge). Both the global and local external work energies were found to be nearly identical for the two test cases, as seen from the relatively small values (<0.4%) in Figure 16. Coincidentally, the two test cases had similar external work values regardless of the differences in applied boundary conditions on the level of the RVE. For the case of the non-periodic boundary conditions, the z-scalar was computed to be a value slightly less than unity. For example, at the last increment of the macroscale analysis (~1% strain) the z-scalar parameter was computed as 0.984. It was hypothesized that this small variation from unity was a function of the test boundary conditions and a lack of significant differences in the RVE response for the periodic and non-periodic BC's. Since periodic boundary conditions have been proven to be energetically consistent, the close agreement between the macroscale periodic and non-periodic external work in Figure 16 would suggest that the implemented z-scalar parameter ensures similar consistency. Also, the small variations seen even with the periodic boundary conditions were hypothesized to be numerical construct within ABAQUS, rather than an imbalance of work between the two scales.

APPLICATION

A case study was undertaken to show an application of z-scalar energy based method. The 2D RVE used for the energy verifications and discussed in the previous sections was used in the following case study. The objective was to investigate the effects of a free edge boundary at the macroscopic level on the constitutive response provided by the RVE. The boundary conditions for the RVE were the test, free-edge boundary conditions proposed in Figure 9-(a). The RVE's constituent properties were those reported in Table II. Again, damage was restricted to fiber/matrix debonding. Fibers were placed into the RVE using an iterative random placement script written in Python, for which the highest achievable fiber volume fraction was 45%. Macroscopic loading was uniaxial tension as in the diagram on Figure 16. Differences between periodic and non-periodic RVE boundary conditions were evaluated according to the macroscopic response (evaluated by plotting the elastic strain energy vs strain) as well as the elastic moduli (E_x, E_y). Previous research works [27,28] have shown that RVE size (number of fibers) affects the macroscopic response, and the appropriate RVE size is dependent on the constituent properties of the RVE. Other works have plotted the variance in macroscopic (stress-strain) response over a variety of boundary conditions, none of which included a free-edge [23,24,26]. In this case study, the RVE size is varied from 4 fibers to 36 fibers with multiple iterations (3-4) of random fiber placement.

Figure 17 plots the elastic strain energy versus macroscopic strain for the 4 fiber RVE, across several random placement iterations, as well as the comparisons between periodic and non-periodic (free) boundary conditions. The curves are labeled according to XPerY or XFreeY, where X is the RVE size and Y is the iteration number. Dashed curves represent the periodic simulations, and solid curves represent those with the non-periodic boundary. The sudden plateaus seen at ~0.6% strain, or

dip in the case of iterations 2 & 3, are a result of the cohesive failure. The curves were as expected from trend seen in the elastic energy curve shown in Figure 15.
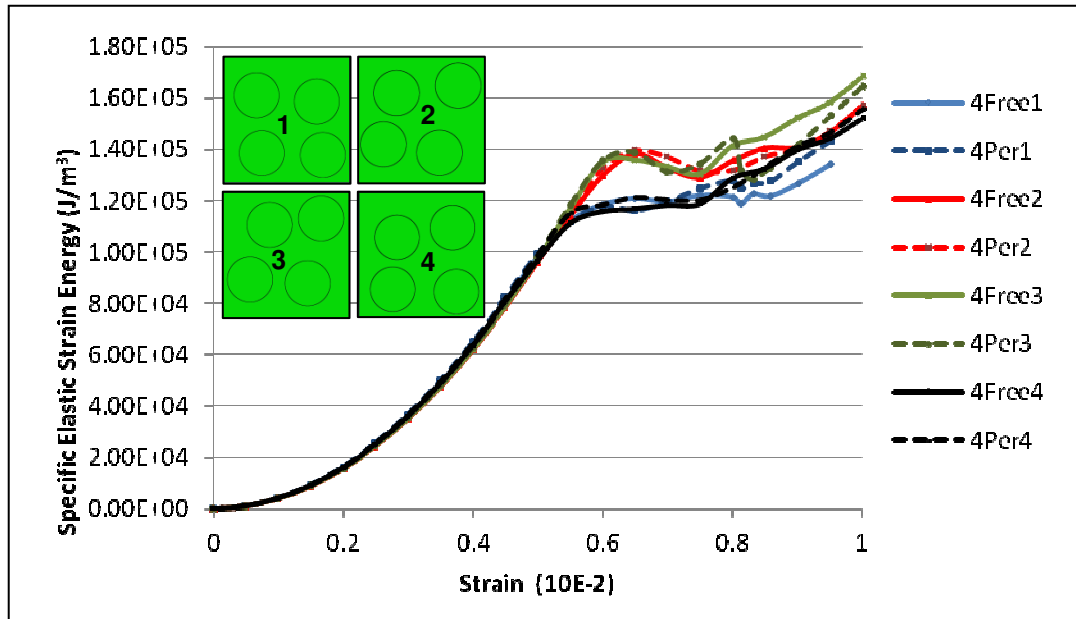

Figure 17. Specific elastic strain energy vs macroscopic strain for the 4-fiber RVE. Dashed lines represent the periodic results, solid lines those of the free edge simulations, and the color coding corresponds to a given RVE iteration.
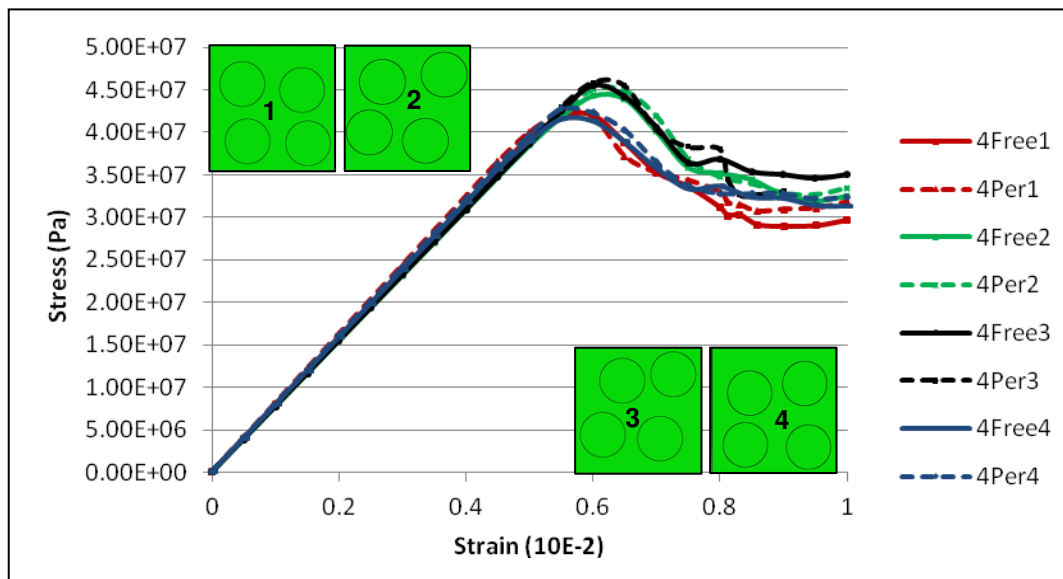

Figure 18. Macroscopic (2-direction) stress vs strain for the 4-fiber RVE.

Figures 18-20 plot the macroscopic stress in the loading (22) direction versus macroscopic strain. These plots provide the RVE's macroscopic material response under the uniaxial tensile loading. For the 4 RVE cases in Figure 18, only one case (iteration 3) had a significantly different response between the two BC's. A similar observation can be made from Figure 17. Figure 18 also highlighted the significant variation in material behavior (cohesive failure) between the 4 different RVE

iterations as a function of the random placement. Iterations 1 & 4 had significantly
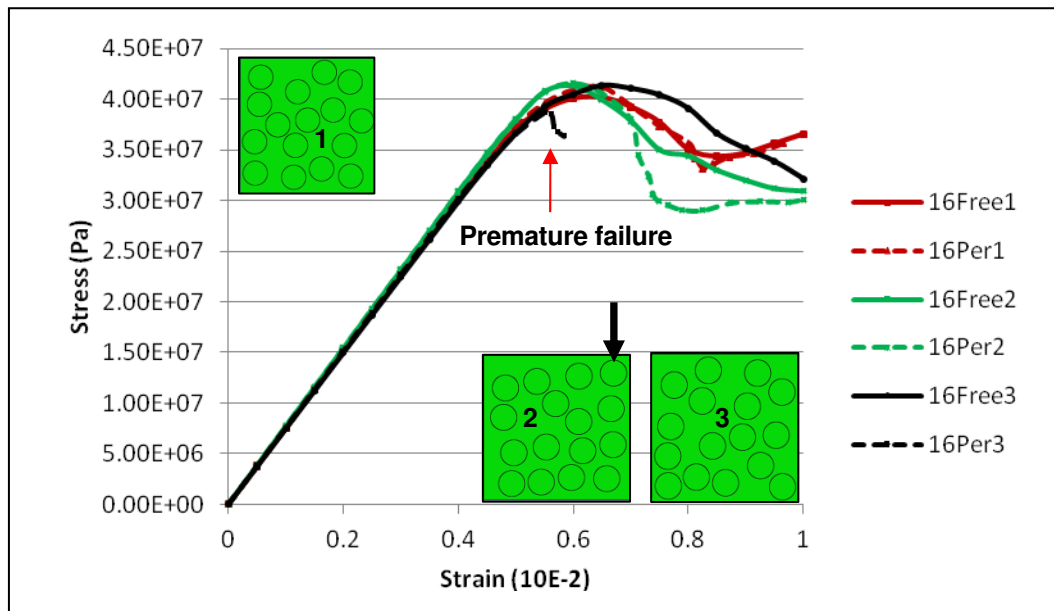

Figure 19. Macroscopic (2-direction) stress vs strain for the 16-fiber RVE.
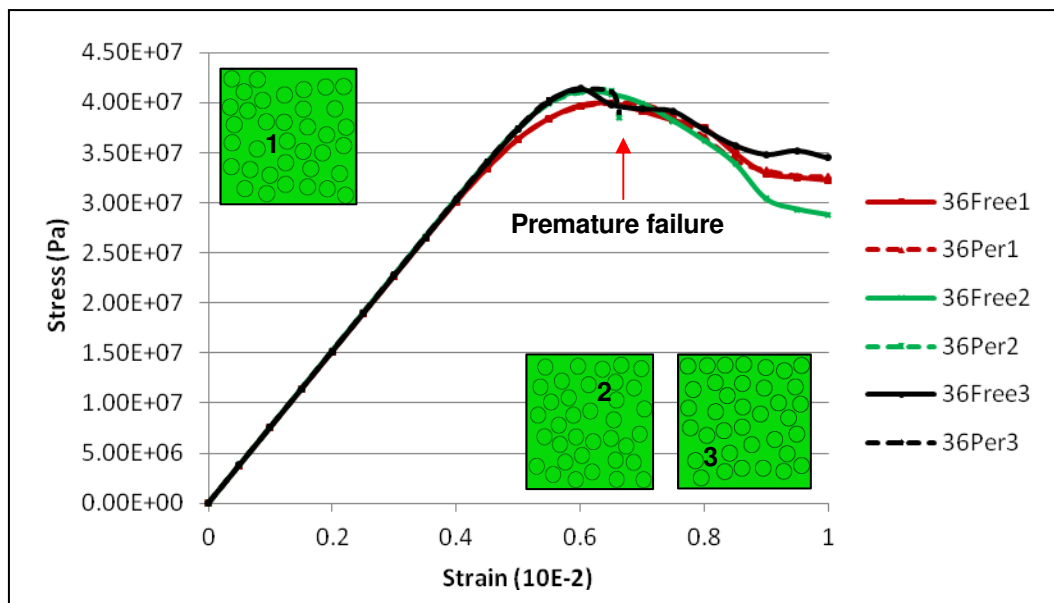
Figure 20. Macroscopic (22 direction) stress vs strain for the 36-fiber RVE.

lower peak stress values (pre-cohesive failure) and a more drastic drop in stress before reloading. Figure 19 shows the results from the 16 fiber test. The simulation for the 16Per3 terminated early due to convergence issues present after cohesive failure and is indicated on the figure. The first 16 fiber RVE iteration had a nearly identical macroscopic response between periodic and non-periodic, while the second iteration had significant softer post-peak response in the periodic BC case. For both of these

iterations, the periodic response was "softer", indicative of increased cohesive damage as a result of the BC. The significant differences in iterations 1 and 2 between the periodic and non-periodic counterparts could be attributed to the RVE fiber placement and effect of the free-edge. The RVE for iteration 1, shown at the top left of Figure 19, had fewer fibers in the proximity of the right-hand edge versus the RVE for iteration 2, shown at the bottom left of the figure. The periodic BC caused cohesive failure and separation at the fiber highlighted by the black arrow on Figure 19, whereas the free edge did not cause failure/separation. The 36 fiber RVE results presented in Figure 20 highlighted two main points. First, as expected from literature, the variation in material macroscopic response decreased across the random fiber iterations. Second, the periodic boundary conditions suffered from numerical convergence issues resulting from premature failure in the cohesive surfaces, highlighted on the figure. This happened for two of the three periodic cases; however, the premature failure did not affect the material's tensile strength as was with the premature failure of the 16Per3 case. The free-edge simulations, however, were able to reach the final macroscopic loading of 1% strain with no issues. Iteration 1, which completed to 1% for both BC's, showed little differences in the macroscopic response. The similarity of periodic and non-periodic response for iteration 1 can again be attributed to the proximity of fibers to the right edge of the RVE, shown at the top-right of Figure 19. Additionally, extracting the initial modulus (slope) from the across the periodic (dashed) and non-periodic (solid) curves in Figures 18-20. First, there was a decrease in variation of the initial modulus within increasing RVE size. The initial modulus converged for the 36 fiber case (6.7 GPa), and was slightly softer than that predicted for the 4 and 16 fiber cases (7.1~6.8 GPa).

CONCLUSION

The developed energy based coupling using the z-scalar method allows one to investigate the effect of non-periodic RVE boundary conditions at the microscale on the global response of the composite. The introduction of a z-scalar parameter allows for the preservation of elastic strain energy between the macroscopic and microscopic domain and is independent of the type of boundary conditions employed on the RVE. The current implementation, however, is limited to a 2D RVE domain, and the formulation of the z-scalar method restricts the RVE to one for which elastic softening is the cause of macroscopic nonlinearity (in this case, cohesive failure).

Despite these current limitations, the robustness of the proposed methodology was shown through a practical investigation of the effect of macroscopic free-edges on the macroscopic response of a 2D fiber/matrix RVE with cohesive interfaces. The results presented suggest that the overall macroscopic response was largely affected by fiber proximity to the free-edge at the microscopic level. A larger number of fibers close to the free-edge result in greater damage evolution from periodic BC's versus non-periodic, free edge BC's. The results suggest that higher fiber volume fraction RVE's, creating an abundance of fibers near the free-edge, would increase the effect of the free-edge to the damage evolution. Namely, a stiffer post-peak response would result from accounting for a macroscopic free-edge.

Future work will develop the z-scalar methodology into a work-based equivalence, rather than elastic strain energy, to allow for plastic deformation and/or

crack growth within the RVE. Applying a work-based form of the z-scalar method and novel BC's will allow for the exploration RVE crack initiation and modeling using XFEM. Appropriate localization schemes will be developed to allow for deformations conducive for crack opening.

ACKNOWLEDGEMENTS

REFERENCES

1. Talreja R., 2006, "Damage analysis for structural integrity and durability of composite materials," Fatigue & Fracture of Engineering Materials & Structures, **29**(7), pp. 481–506.
2. Kanouté P., Boso D. P., Chaboche J. L., and Schrefler B. A., 2009, "Multiscale Methods for Composites: A Review," Archives of Computational Methods in Engineering, **16**, pp. 31–75.
3. Belytschko T., and Song J.-H., 2009, "Coarse-graining of multiscale crack propagation," International Journal for Numerical Methods in Engineering, p. n/a–n/a.
4. Eshelby J. D., 1957, "The Determination of the Elastic Field of an Ellipsoidal Inclusion, and Related Problems," Proceedings of the Royal Society of London. Series A. Mathematical and Physical Sciences, **241**(1226), pp. 376 –396.
5. Mori T., and Tanaka K., 1973, "Average stress in matrix and average elastic energy of materials with misfitting inclusions," Acta Metallurgica, **21**(5), pp. 571–574.
6. Hill R., 1963, "Elastic properties of reinforced solids: Some theoretical principles," Journal of the Mechanics and Physics of Solids, **11**(5), pp. 357–372.
7. Whitney J., and McCullough R., 1990, Micromechanical Materials Modeling, Technomic Publishing Company.
8. Soden P. ., Kaddour A. ., and Hinton M. ., 2004, "Recommendations for designers and researchers resulting from the world-wide failure exercise," Composites Science and Technology, **64**(3–4), pp. 589–604.
9. Ghosh S., Lee K., and Raghavan P., 2001, "A multi-level computational model for multi-scale damage analysis in composite and porous materials," International Journal of Solids and Structures, **38**(14), pp. 2335–2385.
10. Raghavan P., Moorthy S., Ghosh S., and Pagano N. J., 2001, "Revisiting the composite laminate problem with an adaptive multi-level computational model," Composites science and technology, **61**(8), pp. 1017–1040.
11. Rao M. P., Nilakantan G., Keefe M., Powers B. M., and Bogetti T. A., 2009, "Global/Local Modeling of Ballistic Impact onto Woven Fabrics," Journal of Composite Materials, **43**(5), pp. 445–467.
12. Kouznetsova V., 2004, "Computational Homogenization," Graduate School in Mechanics (GraSMech), Eindhoven. Lecture notes.
13. Kouznetsova V. G., Geers M. G. D., and Brekelmans W. A. M., 2004, "Multi-scale second-order computational homogenization of multi-phase materials: A nested finite element solution strategy," Computer Methods in Applied Mechanics and Engineering, **193**(48-51), pp. 5525–5550.
14. Geers M. G. D., Kouznetsova V. G., and Brekelmans W. A. M., 2010, "Multi-scale computational homogenization: Trends and challenges," Journal of computational and applied mathematics, **234**(7), pp. 2175–2182.
15. Feyel F., and Chaboche J. L., 2000, "FE^2 multiscale approach for modelling the elastoviscoplastic behaviour of long fibre SiC/Ti composite materials," Computer methods in applied mechanics and engineering, **183**(3), pp. 309–330.

16. Kalamkarov A. L., Andrianov I. V., and Danishevs'kyy V. V., 2009, "Asymptotic Homogenization of Composite Materials and Structures," Applied Mechanics Reviews, **62**(3), p. 030802.
17. Bednarcyk B. A., 2000, "Modeling woven polymer matrix composites with MAC/GMC."
18. Alfano G., 2006, "On the influence of the shape of the interface law on the application of cohesive-zone models," Composites Science and Technology, **66**(6), pp. 723–730.
19. Volokh K. Y., 2004, "Comparison between cohesive zone models," Communications in Numerical Methods in Engineering, **20**(11), pp. 845–856.
20. Huynh D. B. P., and Belytschko T., 2009, "The extended finite element method for fracture in composite materials," International Journal for Numerical Methods in Engineering, **77**(2), pp. 214–239.
21. Dolbow J., Moës N., and Belytschko T., 2000, "Discontinuous enrichment in finite elements with a partition of unity method," Finite Elements in Analysis and Design, **36**(3–4), pp. 235–260.
22. Van der Sluis O., Schreurs P., Brekelmans W., and Meijer H., 2000, "Overall behaviour of heterogeneous elastoviscoplastic materials: effect of microstructural modelling," Mechanics of Materials, **32**(8), pp. 449–462.
23. Inglis H. M., Geubelle P. H., and Matouš K., 2008, "Boundary condition effects on multiscale analysis of damage localization," Philosophical Magazine, **88**(16), pp. 2373–2397.
24. Coenen E. W. C., Kouznetsova V. G., and Geers M. G. D., 2012, "Novel boundary conditions for strain localization analyses in microstructural volume elements," International Journal for Numerical Methods in Engineering, **90**(1), pp. 1–21.
25. Aboudi J., and Ryvkin M., 2011, "The effect of localized damage on the behavior of composites with periodic microstructure," International Journal of Engineering Science.
26. Larsson F., Runesson K., Saroukhani S., and Vafadari R., 2011, "Computational homogenization based on a weak format of micro-periodicity for RVE-problems," Computer Methods in Applied Mechanics and Engineering, **200**(1-4), pp. 11–26.
27. González C., and LLorca J., 2007, "Mechanical behavior of unidirectional fiber-reinforced polymers under transverse compression: Microscopic mechanisms and modeling," Composites Science and Technology, **67**(13), pp. 2795–2806.
28. Canal L. P., Segurado J., and LLorca J., 2009, "Failure surface of epoxy-modified fiber-reinforced composites under transverse tension and out-of-plane shear," International Journal of Solids and Structures, **46**(11-12), pp. 2265–2274.